Eurographics/ IEEE-VGTC Symposium on Visualization (2007)
Ken Museth, Torsten Möller, and Anders Ynnerman (Editors)

# Visualization Methods for Vortex Rings and Vortex Breakdown Bubbles

Ronald Peikert and Filip Sadlo

ETH Zurich, Switzerland

**Abstract**

*Vortex breakdown bubbles are a subject which is of interest in many disciplines such as aeronautics, mixing, and combustion. Existing visualization methods are based on stream surfaces, direct volume rendering, tensor field visualization, and vector field topology. This paper presents a topological approach which is more closely oriented at the underlying theory of continuous dynamical systems. Algorithms are described for the detection of vortex rings and vortex breakdown bubbles, and for visualization of their characteristic properties such as the boundary, the chaotic dynamics, and possible islands of stability. Since some of these require very long streamlines, the effect of numerically introduced divergence has to be considered. From an existing subdivision scheme, a novel method for divergence conserving interpolation of cuboid cells is derived, and results are compared with those from standard trilinear interpolation. Also a comparison of results obtained with and without divergence cleaning is given.*

Categories and Subject Descriptors (according to ACM CCS): I.3.8 [Computer Graphics]: Applications

## 1. Introduction

The current popularity of vector field topology in visualization is to a large extent due to its capability of automatically segmenting 2D vector fields into regions of similar flow behavior. For the segmentation it is enough to compute the topological skeleton which is the set of all critical points (i.e. isolated zeros) and all stable and unstable manifolds of saddle points. The stable manifold of a point $P$ is the set $W^s(P)$ of points from where a streamline converges to $P$ with time $t \to \infty$. The unstable manifold $W^u(P)$ is defined likewise but with $t \to -\infty$. For saddle points in a 2D vector field these manifolds are also known as the separatrices.

From a theoretical point of view, the 3D case is not much different. The role of the saddle points is now taken by the 3D saddles and the spiral saddles (saddle foci), as defined, e.g. in [Asi93]. And their stable and unstable manifolds now come in a pair of a 1D and a 2D manifold. The 2D manifolds, which are special stream surfaces, provide again a segmentation of the field. In practice, however, this has not yet proved very successful, except perhaps for irrotational vector fields. One reason for this is of course the occlusion problem which forbids to display dozens of stream surfaces. A possible solution is to display not the stream surfaces themselves, but only their pairwise intersections, known as saddle connectors [TWHS03]. But even if there are just a few critical points (two are sufficient), a skeleton can result which has very convoluted stream surfaces. In the case of divergence-free vector fields, this is often due to the well known chaotic phenomenon first described by Shilnikov [Sil65] and explained in Section 2. But also if the field has some amount of divergence, Shilnikov chaos can be observed.

As an approach to solve this problem, we propose not to use the full stream surfaces required by the skeleton, but only specific parts of them. We will show later how by combining parts of stream surfaces, a systematic visualization of recirculations can be achieved. While on the one hand we argue for a restriction of the skeleton, we extend it on the other hand by the periodic orbits because a topological skeleton based on critical points alone gives an incomplete picture. This can be seen already in two dimensions, whenever the vector field contains periodic orbits. Periodic orbits can be attractors or repellors and thus behave like sinks or sources. In three dimensions, periodic orbits are even more relevant since they can also be of saddle type. In this case they have a pair of 2D (un-)stable manifolds which behave much like separatrices in 2D vector fields and therefore should not be

neglected in the topological skeleton. Figure 15 shows an example of such a case. It can be said that with increasing dimensionality, the variety of topological phenomena also increases, and therefore the need to include more than critical points into the visualization. While in 2D, attractors can be critical points or periodic orbits, in 3D two more types exist, namely invariant tori and strange attractors. It could be argued that a "complete" topological skeleton should contain all lower-dimensional stable and unstable manifolds of any type of attractor.

While vector field topology, initiated by Helman and Hesselink [HH89], builds on the underlying theory of continuous dynamical systems (see e.g. [GH83]), only a small part of the latter has been explored for the purpose of visualization. Critical points clearly received most attention in visualization of both flow data [GLL91] and dynamical systems [LDG98]. But also Poincaré maps were shown to be useful for visualization [Loe98]. It is a goal of this paper to demonstrate that by borrowing more concepts from dynamical systems theory more structure can be detected and visualized, not only in synthetic flow fields but also in industrial CFD results.

Vortex breakdown bubbles in CFD data have been observed and visualized by Garth et al. [GTS*04a, GTS04b] using techniques based on stream surfaces, and by tracking the pairs of critical points associated with this structure. Tricoche et al. [TGK*04] used direct volume rendering for visualization and vector field topology in planar slices for extracting periodic orbits. Rütten and Chong [RC06] developed a visualization method based on tensor field color coding. In this paper we propose techniques based on Poincaré maps which exploit the special topology of vortex rings. They can robustly and automatically handle features such as non-isolated periodic orbits within nested tori, periodic orbits of higher periodicities, and stream surfaces with strong folding, which are difficult to treat with general-purpose methods.

## 2. Background on Vortex Rings

A simple model of a vortex ring consists of a set of nested tori on which all streamlines have to lie. In the simplest topological case, the nested tori are bounded on the inner side by a periodic orbit and on the outer side by a sphere-like surface. If we further assume that the vortex ring has nonvanishing swirl, (rotational component around the axis of the tori), the whole structure has only two critical points. They are of spiral saddle (saddle focus) type, and they are located where the axis intersects the outer boundary. If the tori are allowed to have non-circular cross sections, then such vortex models can be physically valid, i.e. be solutions of Navier-Stokes equations. Examples are Hill's vortex (see [Saf92]) and Norbury's vortex rings [Nor73]).

Nevertheless, this ideal topology of a vortex ring is usually not found in practical velocity fields. The reason is that it requires the 2D unstable manifold of the one critical point to exactly coincide with the stable manifold of the other, and likewise for the pair of 1D manifolds, a configuration which is not structurally stable. In a perturbed version of this ideal vortex ring, the 2D manifolds do not exactly match, which means that the boundary is not "water-tight" or that the recirculation is not perfect. On the inner side, the 1D manifolds do not coincide either, so that the axis of the structure is no more well defined in a topological sense. As a side remark, this is a nice example of a vortex whose core line is not a streamline.

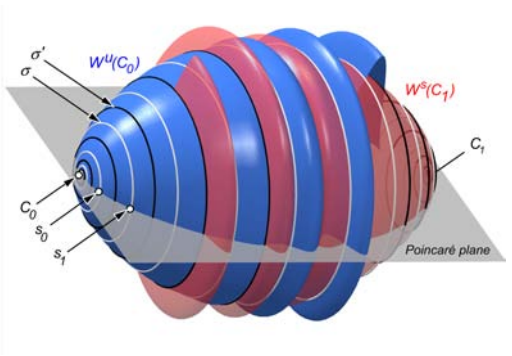


**Figure 1:** *Unstable manifold (blue) and stable manifold (red) of spiral saddles $C_0$ and $C_1$, respectively, intersecting in saddle connectors $\sigma$ and $\sigma'$. In a Poincaré plane through $C_0$ and $C_1$, the seed curve for integration is chosen between two successive intersection points $s_0$ and $s_1$ of $\sigma$.*

If the vector field is divergence-free, e.g. because of an incompressible fluid, the effect of a perturbation is even more dramatic. In divergence-free 3D vector fields with sufficient swirl, any transversal intersection of the 2D (un-)stable manifolds of two spiral saddles automatically implies the so-called Shilnikov chaos [Sil65]. This is illustrated in Figure 1, where $C_0$ is a 1:2 spiral saddle and $C_1$ is a 2:1 spiral saddle. In general, the 2D (un-)stable manifolds of such critical points do not coincide, but intersect transversally. In this case they intersect at an even number of saddle connectors (heteroclinic orbits), usually a pair $\sigma$ and $\sigma'$ of them. Between the windings of the saddle connectors, the manifolds form two "tubes" that are wrapped around the structure. The tubes have constant flux (i.e. independent of cross sections) because the 2D manifolds are stream surfaces, and the sum of the two fluxes is zero because of the divergence-free condition. This implies that near the critical points, where velocities approach zero, the tubes must either have increasing cross section area or develop folds which extend into regions of higher velocities. While a vortex breakdown bubble and a smoke ring are two different physical phenomena, from a topological point of view, they can both be treated as vortex rings.

The definition of stable and unstable manifolds requires

either a steady or an instantaneous vector field. This raises the question about their relevance for time-dependent flows, especially if they are chaotic and thus require long integration time. The answer is that practical flow often has small enough time-dependence that their visualization as steady flow is a good enough approximation. Vortex rings and, in particular, vortex breakdown bubbles have been photographed in experiments (see Figure 2) and their shape has been shown to be consistent with the manifolds of critical points in a steady vector field [SVL01].

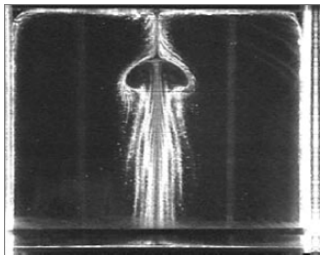

**Figure 2:** *Photograph of vortex breakdown bubble in experiment. Image copied with permission from [SMH98].*

## 3. Detection of Vortex Rings

Our strategy for finding vortex rings is to look for pairs of critical points, one of them being a 1:2 spiral saddle and one a 2:1 spiral saddle. The number of such candidate pairs can be reduced by imposing a maximal distance. Additionally, it can be demanded that they lie on a common vortex core line. Each candidate pair of critical points is then checked for defining a vortex ring. For this purpose, a Poincaré section is taken by using a plane passing through the two points. The 2D (un-)stable manifold of the spiral saddle is now computed based on a discrete set of seed points and the intersections of the manifold with the Poincaré section are stored as a (texture) image. The extent of the grid is chosen based on the distance $d$ between the two critical points. We found a square with edge length $2d$ to be sufficient in most cases.

Seed points for the manifold of, say, $C_0$ are generated as follows (see Figure 1). A first seed $s_0$ is chosen at a small offset from $C_0$ on the Poincaré plane where it intersects the plane spanned by the two complex eigenvectors. From $s_0$ a streamline is integrated in the time direction where the distance from $C_0$ increases. Its next iterate (i.e. intersection with the Poincaré plane) is denoted by $s_1$. Further seed points are now generated on the straight line segment between $s_0$ and $s_1$ by logarithmically interpolating the distance of the seed points to $C_0$. Logarithmic interpolation is appropriate because streamlines of the linearized vector field at $C_0$ are logarithmic spirals, and the error introduced by interpolating along a straight line falls off with the streamlines converging to the 2D manifold.

The resulting image (Figure 3 is an example) then shows

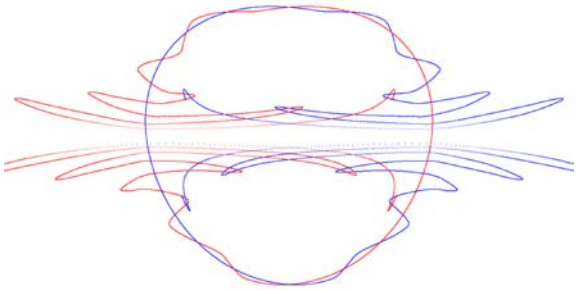

**Figure 3:** *Planar section of 2D manifolds of a synthetic vortex breakdown bubble.*

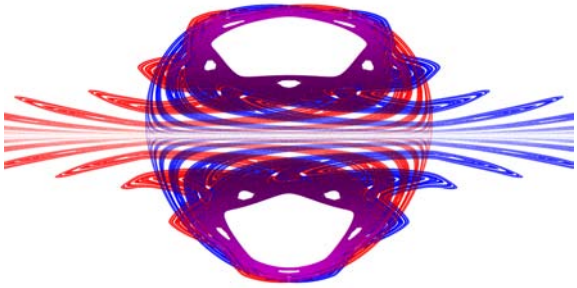

**Figure 4:** *Manifolds of Figure 3 at longer integration time.*

a section of the manifold with its folds, also called lobes, extending toward the second critical point. In the image plane, it is easily possible to check for an intersection of the two curves. If an intersection is detected, the vortex ring is verified and ready for its visualization.

One way of visualizing the vortex ring is to increase the integration time until the inner structure becomes visible on the Poincaré section, as is depicted in Figure 4. The resulting image shows the chaotic region formed by the inward folding lobes, and it typically shows a hierarchy of islands of stability. The islands of stability are toroidal regions around a periodic orbit of minimal period. The inner part of stability islands is typically filled with nested invariant tori with no flux across them.

Islands of stability can be visualized by showing their outer boundary and/or their center periodic orbit. The periodic orbit can be located as usual by searching for fixed points in the Poincaré map. A faster algorithm exploiting the given structure of nested tori in islands of stability is presented in [PS07] where also a method for computing the approximate boundary of the island is described. These points and curves in the Poincaré section can further be used as

integration seeds, giving a 3D visualization of the periodic orbits and invariant tori, respectively.

## 4. Computing a Boundary Surface

A practically useful result for pairs of spiral saddles is that the recirculation zone defined by such a pair can be visualized by a boundary surface constructed from the 2D (un-) stable manifolds. The boundary is made up of two stream surfaces and can be closed by adding a so-called *turnstile* [MMP84] which is usually small and which is the only place where flux through the surface can occur.

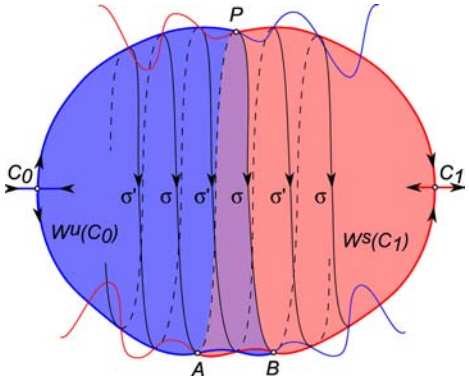


**Figure 5:** *Poincaré section of unstable (blue) and stable (red) manifolds. The manifolds are joined at P, resulting in a turnstile between A and B.*

In Figure 5 it is shown how a boundary of a (perturbed) vortex ring is obtained. First, the intersection of the 2D manifolds $W^u(C_0)$ and $W^s(C_1)$ with a Poincaré section are computed (shown as red and blue curves). Then an intersection point $P$ is found at which the two curves are trimmed and joined into one.

The criterion for the choice of $P$ is to minimize the total arc length of the curve $C_0 - P - C_1$. For an approximate solution we use the following greedy algorithm: Starting with the curve segment between the seeds $s_0$ and $s_1$, compute successive iterates of the segment and add it to the curve.

The obtained segments have the same frequency as the lobes (corresponding to a cycle of hues in Figure 6), with a possible phase shift. This process of extending a curve is done in an interleaved way with both curves, such that the arc lengths of the two next segments are compared and the shorter of the two is used.

Having now a seed curve, a stream surface is integrated backward and forward until the section plane is intersected again. Under these "half turn" ($\pi$-period) Poincaré maps the curve $C_0 - P - C_1$ is mapped to $C_0 - A - C_1$ and $C_0 - B - C_1$, respectively. The two curves coincide with the exception of their parts between $A$ and $B$. Therefore the stream surface is closed, up to the figure eight shaped opening lying in the Poincaré section plane between the points $A$ and $B$. This opening, the turnstile, consists of an inflow and an outflow having equal absolute flux if the field is divergence-free. The influx (or outflux) can be easily computed and it tells what fraction of the enclosed fluid is exchanged per time unit. In practical cases, the turnstile is often very small. Figures 6 and 7 show the two manifolds for the application example of Section 6.1 and Figure 8 shows the resulting seed curve. When starting from here, stream surface integration yields the boundary of the vortex ring shown in Figures 9 and 10.

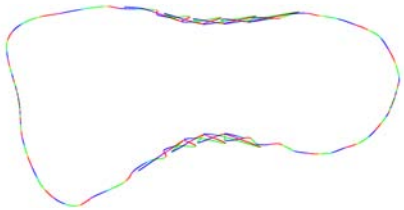

**Figure 6:** *Section of the manifolds of the vortex ring in the Francis draft tube.*

**Figure 7:** *Close-up of Figure 6.*

**Figure 8:** *Manifolds after trimming at selected intersection point, minimizing the maximal size of the lobes.*

## 5. Vortex Rings in Discrete Data

From a topological aspect, the divergence-free case is particularly interesting, as already mentioned in the introduction. However, when discrete data are used, divergence can be artificially introduced by the interpolation method. Furthermore, the data may have some residual divergence. And, finally, they may be divergence-free only with respect to the dual grid, as is the case for finite volumes solutions. We describe now two techniques that can be applied to cope with these problems.

### 5.1. Divergence Cleaning

For a divergence-free field, the total flux through the boundary of a volume element is zero by Gauss' theorem. However, if the data set is a finite volumes solution, this holds for the control volumes, but not necessarily for the grid cells if standard multilinear interpolation is assumed. The control volumes are in general more complex polyhedra than hexahedra or tetrahedra, so it is usually not an option to use the

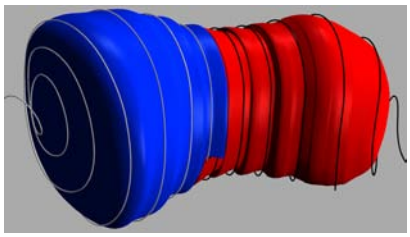

**Figure 9:** *Unstable manifold (blue) and stable manifold (red) rendered as stream surfaces. Streamlines entering (white) and leaving (black) the recirculation region.*

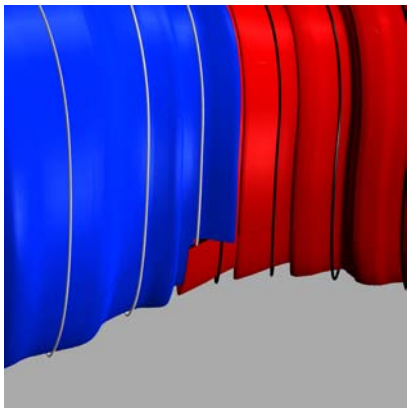

**Figure 10:** *Close-up of Figure 9*

control volumes as the visualization grid. Instead, we keep the original grid, or resample it to a rectilinear (possibly nonuniform) grid if necessary.

Divergence cleaning methods [BK03] were developed mostly within the field of magnetohydrodynamics. One of them is the Hodge projection [Tot00] which removes divergence based on the decomposition $\mathbf{u} = \mathbf{u}_0 + \nabla s$ of $\mathbf{u}$ into a divergence-free part $\mathbf{u}_0$ and an irrotational part $\nabla s$. It follows $\nabla \cdot \mathbf{u} = \nabla \cdot \nabla s$ which is a Poisson equation for $s$. Effectively, the flux of each cell is distributed to its neighbor cells by making small changes to the vector data at the grid nodes. These changes can be minimized either in the absolute or relative sense.

### 5.2. Divergence Conserving Interpolation

Let us assume now a rectilinear 3D grid which is divergence-free in the sense that for each cell the trilinear interpolant has zero flux through its boundary. Unfortunately, this does not mean that the trilinear interpolant has zero divergence at all inner points. It is instead necessary to use a divergence conserving interpolation scheme. Tóth and Roe [TR02] describe how a hexahedral grid can be subdivided such that the zero flux property is conserved. By iterating this approach a few times followed by trilinear interpolation, one could get interpolated field values with sufficiently small divergence. We found however that Tóth and Roe's technique can be modified to generate instead of a subdivision a tetrahedral decomposition with the property that the piecewise linear interpolant is exactly divergence conserving.

Starting with the 2D case, we consider a rectangular cell with edge lengths $s_x$ and $s_y$. Let $(u_{ij}, v_{ij})(i, j = 0, 1)$ be the velocity vectors at the cell corners. Assuming bilinear interpolation, the total flux out of the cell is:

$$\Phi = \frac{1}{2} \sum_{p=0,1} \left(u_{1p} - u_{0p}\right) s_y + \left(v_{p1} - v_{p0}\right) s_x \qquad (1)$$

The divergence of the bilinear interpolant is not constant in general. In particular, even if $\Phi = 0$, the divergence is not necessarily zero. However, after splitting the cell into four triangles a piecewise linear interpolant can be found which has constant divergence $\frac{\Phi}{s_x s_y}$. For this, the velocity at the cell center must be set to

$$\begin{aligned} u_{\frac{1}{2}\frac{1}{2}} &= \tfrac{1}{4} \sum_{i,j=0,1} u_{ij} + (-1)^{i+j} \tfrac{s_x}{s_y} v_{ij} \\ v_{\frac{1}{2}\frac{1}{2}} &= \tfrac{1}{4} \sum_{i,j=0,1} v_{ij} + (-1)^{i+j} \tfrac{s_y}{s_x} u_{ij} \end{aligned} \qquad (2)$$

These expressions for $u_{\frac{1}{2}\frac{1}{2}}$ and $v_{\frac{1}{2}\frac{1}{2}}$ can be found by symbolically solving the four equations which are obtained by setting the divergence in each of the four triangles to $\frac{\Phi}{s_x s_y}$. It turns out that the rank of this linear system is two, hence there is a unique solution.

For the 3D case, consider now a cuboid cell with edge lengths $s_x$, $s_y$ and $s_z$. Let $(u_{ijk}, v_{ijk}, w_{ijk})(i, j, k = 0, 1)$ be the velocity vectors at the cell corners. For trilinear interpolation, the total flux out of the cell is

$$\begin{aligned} \Phi = \tfrac{1}{4} \sum_{p,q=0,1} &\left(u_{1pq} - u_{0pq}\right) s_y s_z + \left(v_{q1p} - v_{q0p}\right) s_z s_x \\ &+ \left(w_{pq1} - w_{pq0}\right) s_x s_y \end{aligned} \qquad (3)$$

Again, a piecewise linear interpolation can be found which has constant divergence within the entire cell. For this, the hexahedral cell has to be split into 24 tetrahedra, given by the six face centers and the cell center in addition to the vertices. At the face centers, the velocity field is interpolated analogous to (2), e.g. for the two $k = const$ faces:

$$\begin{aligned} u_{\frac{1}{2}\frac{1}{2}k} &= \tfrac{1}{4} \sum_{i,j=0,1} u_{ijk} + (-1)^{i+j} \tfrac{s_x}{s_y} v_{ijk} \\ v_{\frac{1}{2}\frac{1}{2}k} &= \tfrac{1}{4} \sum_{i,j=0,1} v_{ijk} + (-1)^{i+j} \tfrac{s_y}{s_x} u_{ijk} \\ w_{\frac{1}{2}\frac{1}{2}k} &= \tfrac{1}{4} \sum_{i,j=0,1} w_{ijk} \end{aligned} \qquad (4)$$

Note, that correction terms appear only in the $u$ and $v$ components, while the $w$-component is computed as in the standard trilinear interpolation. As a consequence, the flux through the $k = const$ faces remains unchanged. The expressions for the two other pairs of faces are obtained by cyclic permutation.

At the cell center, the velocity vector must be set to

$$u_{\frac{1}{2}\frac{1}{2}\frac{1}{2}} = \frac{1}{8}\sum_{i,j,k=0,1} u_{ijk} + (-1)^{i+j}\frac{s_x}{s_y}v_{ijk} + (-1)^{i+k}\frac{s_x}{s_z}w_{ijk}$$
$$v_{\frac{1}{2}\frac{1}{2}\frac{1}{2}} = \frac{1}{8}\sum_{i,j,k=0,1} v_{ijk} + (-1)^{j+k}\frac{s_y}{s_z}w_{ijk} + (-1)^{j+i}\frac{s_y}{s_x}u_{ijk}$$
$$w_{\frac{1}{2}\frac{1}{2}\frac{1}{2}} = \frac{1}{8}\sum_{i,j,k=0,1} w_{ijk} + (-1)^{k+i}\frac{s_z}{s_x}u_{ijk} + (-1)^{k+j}\frac{s_z}{s_y}v_{ijk} \quad (5)$$

Again, these expressions are found as the unique solution of a linear system.

Formulas (2), (4) and (5) for velocities at face centers and cell centers are closely related to those derived by Tóth and Roe [TR02]. They have the property that when a cubic cell is subdivided into eight cubic subcells, the total flux is evenly distributed to the eight subcells. But subdividing a cell with zero flux does not provide zero divergence in the interior, therefore this scheme is not applicable for our purpose. Tóth and Roe's expressions differ in the correction terms which are scaled by $\frac{1}{2}$ and $\frac{3}{2}$, respectively.

## 6. Results

### 6.1. Vortex Ring in Francis Draft Tube

Our first application example, which we used already in Section 4, is a transient simulation of the flow in the draft tube of a Francis turbine. After passing the bend and the divider, the flow forms a large spanwise vortex as can be seen in Figure 11. This was found by extracting vortex core lines and analyzing nearby critical points as described in Section 3.

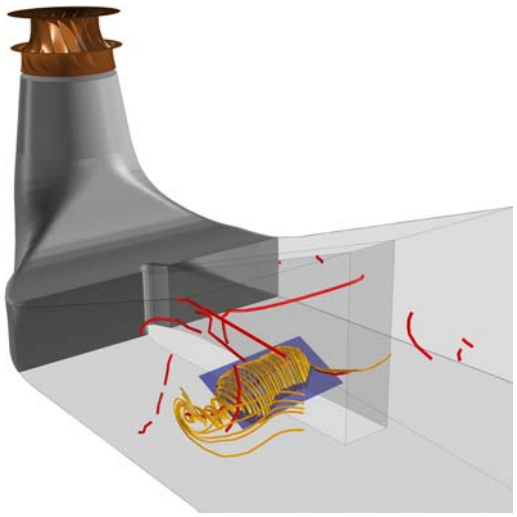

**Figure 11:** *Vortex ring in Francis draft tube with section plane (blue), streamlines (yellow) and vortex core lines (red).*

For a selected time step, we compared the effect of divergence cleaning and of two choices of the interpolation function. For the numerical integration, the fourth-fifth-order Runge-Kutta-Fehlberg procedure from the Netlib library was used in all cases. In Figure 12, the manifolds of the original data (white) and the divergence-cleaned data (colored) are shown. In both cases, standard trilinear interpolation was used. Figure 13 shows the same manifolds, but computed using divergence conserving interpolation. It can be observed, that the choice of the interpolation scheme has little impact for short integration times. The two white curves are identical up to pixel resolution, and also the outer boundary of the colored manifolds coincide. However, the long-time behavior of the manifold is affected by the interpolation method. With trilinear interpolation, one of the two islands of stability is filled up with streamlines being attracted to a periodic orbit in its center. More important than the interpolation scheme is the use of divergence cleaning. Even though the CFD data represent an incompressible fluid, without a divergence cleaning as a preprocessing, the vector field has strong enough attracting and repelling behavior to let most of the chaotic structure disappear. This is the reason why in an earlier paper [PS05] a vortex ring was found (Figure 10)

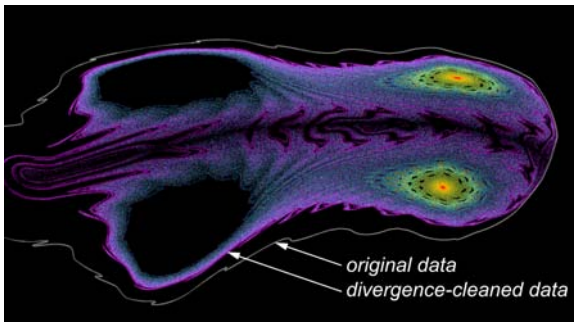


**Figure 12:** *Unstable manifold computed in trilinearly interpolated field. Comparison of original data (white) and divergence-cleaned data (colored).*

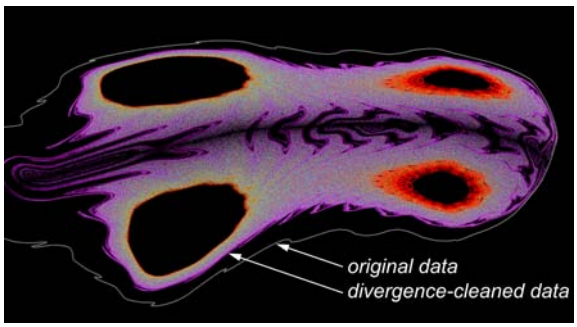


**Figure 13:** *Unstable manifold computed in divergence-conservingly interpolated field. Comparison of original data (white) and divergence-cleaned data (colored).*

which exhibits some amount of folding although the pair of 2D manifolds did not intersect.

The recirculation region under examination exhibits a temporally quite stable behavior. Its lifespan extends over 116 of total 301 time steps. At time step 90, a split event occurs where the shape transforms into a figure eight shape (in the section plane) and breaks apart, i.e. a double critical point is created which then separates into two single ones. At time step 94, the smaller of the two structures collapses, and at time step 115 the larger collapses, too.

### 6.2. Vortex Ring in Simulation of a River Power Plant

While the extraction of the vortex ring was done in a fully automatic way for more than 100 time steps in the previous example, there are topologically more complex cases. In this example, the flow in the intake of a river power plant was simulated (see Figure 14) assuming a planar[†] water surface.

The selected vortex ring extends to the (free slip) water surface where one of the two spiral saddles ($C_1$ in Figure 15) is located. The unstable manifold of the latter coincides with the stable manifold of a periodic orbit $P$ of saddle type which is also located at the water surface. In order to prevent streamlines from leaving the domain, the vertical velocity component at the water surface had to be set to exactly zero, i.e. residual $z$-velocities from the simulation had to be removed. Then, because $W^u(C_1)$ converges to a periodic orbit, the criterion of intersecting 2D manifolds is not fulfilled, resulting in a failure of the automatic detection. We circumvented this problem by giving the seed curve a small downward offset. For a systematic approach, one could in such a case proceed with the unstable manifold of the periodic orbit $W^u(P)$, which means, however, to examine two cases, since in general the unstable manifold extends in two directions.

The apparent join of pairs of lobes below $C_0$ is an artifact of the planar section. If a non-planar section following the curved center line of the structure were taken, a picture looking more like Figure 4 would have resulted.

## 7. Conclusion

We presented a method for detecting and visualizing vortex rings and vortex breakdown bubbles in vector fields. The assumptions made are that the recirculation region is characterized by a pair of critical points of spiral saddle type, and that these are connected by saddle connectors which have a sufficient amount of spiraling. When applied to hydrodynamics CFD results, where such a configuration is likely to produce chaotic dynamics, this is revealed by our method. Once a vortex ring has been detected, a boundary surface is computed by combining parts of the 2D (un-) stable manifolds of the two critical points. The position of the turnstile on the boundary surface is chosen by minimizing the size of its lobes. Furthermore, we provided a method for divergence-conserving piece-wise linear interpolation of cuboid cells. And finally, we analyzed the effect of using divergence cleaning and/or divergence-conserving interpolation on vortex-rings in two cases of industrial CFD data.

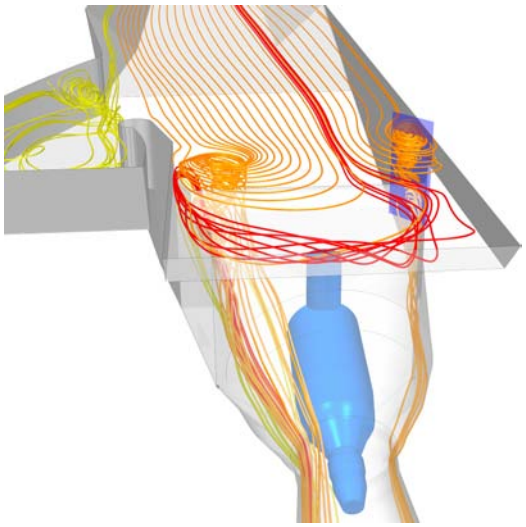

**Figure 14:** *Overview of the flow in the river power plant. Poincaré section shown as blue rectangle.*

[†] In a newer simulation, the water-air interface was simulated, too, resulting in a more realistic water surface

### Acknowledgment

We thank VA Tech Hydro for the draft tube data and France Suerich-Gulick for the river power plant data. This work was supported by the Swiss Commission for Technology and Innovation (CTI) under grant 7338.2 ESPP-ES.

### References

[Asi93] ASIMOV D.: *Notes on the Topology of Vector Fields and Flows*. Tech. Rep. RNR-93-003, NASA Ames Research Center, 1993.

[BK03] BALSARA D., KIM J.: An intercomparison between divergence-cleaning and staggered mesh formulations for numerical magnetohydrodynamics. *Eprint Astrophysics astro-ph/0310728* (2003).

[GH83] GUCKENHEIMER J., HOLMES P.: *Nonlinear Oscillations, Dynamical Systems and Bifurcations of Vector Fields*. Applied Mathematical Sciences, Vol. 42. Springer, New York, Berlin, Heidelberg, Tokyo, 1983.

[GLL91] GLOBUS A., LEVIT C., LASINSKI T.: A tool for visualizing the topology of three-dimensional vector fields. In *VIS '91: Proceedings of the 2nd conference on*

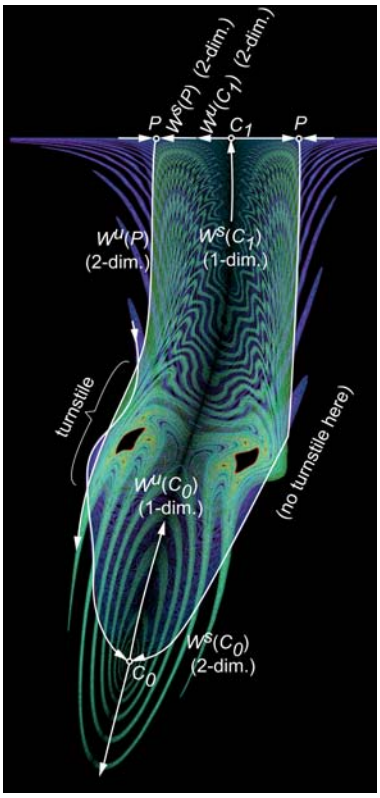


**Figure 15:** *Both manifolds of vortex in river power plant.*

*Visualization '91* (Los Alamitos, CA, USA, 1991), IEEE Computer Society Press, pp. 33–40.

[GTS*04a] GARTH C., TRICOCHE X., SALZBRUNN T., BOBACH T., SCHEUERMANN G.: Surface techniques for vortex visualization. In *VisSym* (2004), pp. 155–164, 346.

[GTS04b] GARTH C., TRICOCHE X., SCHEUERMANN G.: Tracking of vector field singularities in unstructured 3d time-dependent datasets. In *VIS '04: Proceedings of the conference on Visualization '04* (Washington, DC, USA, 2004), IEEE Computer Society, pp. 329–336.

[HH89] HELMAN J., HESSELINK L.: Representation and display of vector field topology in fluid flow data set. *IEEE Computer* (August 1989), 27–36.

[LDG98] LÖFFELMANN H., DOLEISCH H., GRÖLLER E.: Visualizing dynamical systems near critical points. In *14th Spring Conference on Computer Graphics* (April 1998), Kalos L. S., (Ed.), pp. 175–184.

[Loe98] LOEFFELMANN H.: *Visualizing Local Properties and Characteristic Structures of Dynamical Systems*. Dissertation, 1998.

[MMP84] MACKAY R. S., MEISS J. D., PERCIVAL I. C.: Transport in hamiltonian systems. *Physica D 13D* (1984), 55–81.

[Nor73] NORBURY J.: A family of steady vortex rings. *J. Fluid Mech. 57, Pt. 3* (1973), 417–431.

[PS05] PEIKERT R., SADLO F.: Topology-guided visualization of constrained vector fields. In *Proceedings of the 2005 Workshop on Topology-Based Methods in Visualization, Budmerice, Slovakia* (2005).

[PS07] PEIKERT R., SADLO F.: Flow topology beyond skeletons: Visualization of features in recirculating flow. In *submitted to: 2007 Workshop on Topology-Based Methods in Visualization, Leipzig, Germany* (2007).

[RC06] RUETTEN M., CHONG M.: Analyzing vortex breakdown flow structures by assignment of colors to tensor invariants. *IEEE Transactions on Visualization and Computer Graphics 12, no. 5* (2006), 1189–1196.

[Saf92] SAFFMAN P. G.: *Vortex Dynamics*. Cambridge Univ. Press, Cambridge, UK, 1992.

[Sil65] SIL'NIKOV L. P.: A case of the existence of a denumerable set of periodic motions. *Sov. Math. Dokl. 6* (1965), 163–166.

[SMH98] SPOHN A., MORY M., HOPFINGER E.: Experiments on vortex breakdown in a confined flow generated by a rotating disc. *Journal of Fluid Mechanics 370* (1998), 73–99.

[SVL01] SOTIROPOULOS F., VENTIKOS Y., LACKEY T. C.: Chaotic advection in three-dimensional stationary vortex-breakdown bubbles: Sil'nikov's chaos and the devil's staircase. *J. Fluid Mech. 444* (2001), 257–297.

[TGK*04] TRICOCHE X., GARTH C., KINDLMANN G., DEINES E., SCHEUERMANN G., RUETTEN M., HANSEN C.: Visualization of intricate flow structures for vortex breakdown analysis. In *VIS '04: Proceedings of the conference on Visualization '04* (Washington, DC, USA, 2004), IEEE Computer Society, pp. 187–194.

[Tot00] TOTH G.: The div b=0 constraint in shock-capturing magnetohydrodynamics codes. *Journal of Computational Physics 161* (2000), 605–652.

[TR02] TÓTH G., ROE P. L.: Divergence- and curl-preserving prolongation and restriction formulas. *J. Comput. Phys. 180*, 2 (2002), 736–750.

[TWHS03] THEISEL H., WEINKAUF T., HEGE H.-C., SEIDEL H.-P.: Saddle connectors - an approach to visualizing the topological skeleton of complex 3d vector fields. In *Proc. IEEE Visualization 2003* (Seattle, U.S.A., October 2003), Turk G., van Wijk J. J., Moorhead R., (Eds.), pp. 225–232.